



**HAL**  
open science

# Hydrodynamic torque on a slender cylinder rotating perpendicularly to its symmetry axis

Jean-Lou Pierson, Mohammed Kharrouba, Jacques Magnaudet

► **To cite this version:**

Jean-Lou Pierson, Mohammed Kharrouba, Jacques Magnaudet. Hydrodynamic torque on a slender cylinder rotating perpendicularly to its symmetry axis. *Physical Review Fluids*, 2021, 6 (9), pp.094303. 10.1103/PhysRevFluids.6.094303 . hal-03356843

**HAL Id: hal-03356843**

**<https://hal.science/hal-03356843v1>**

Submitted on 28 Sep 2021

**HAL** is a multi-disciplinary open access archive for the deposit and dissemination of scientific research documents, whether they are published or not. The documents may come from teaching and research institutions in France or abroad, or from public or private research centers.

L'archive ouverte pluridisciplinaire **HAL**, est destinée au dépôt et à la diffusion de documents scientifiques de niveau recherche, publiés ou non, émanant des établissements d'enseignement et de recherche français ou étrangers, des laboratoires publics ou privés.





[Open Archive Toulouse Archive Ouverte](#)

OATAO is an open access repository that collects the work of Toulouse researchers and makes it freely available over the web where possible

This is an author's version published in: <http://oatao.univ-toulouse.fr/28275>

**Official URL :** <https://doi.org/10.1103/PhysRevFluids.6.094303>

**To cite this version:**

Pierson, Jean-Lou and Kharrouba, Mohammed  and Magnaudet, Jacques   
*Hydrodynamic torque on a slender cylinder rotating perpendicularly to its symmetry axis.* (2021) Physical Review Fluids. ISSN 2469-990X

Any correspondence concerning this service should be sent to the repository administrator: [tech-oatao@listes-diff.inp-toulouse.fr](mailto:tech-oatao@listes-diff.inp-toulouse.fr)

# Hydrodynamic torque on a slender cylinder rotating perpendicularly to its symmetry axis

Jean-Lou Pierson,<sup>1,\*</sup> Mohammed Kharrouba,<sup>2</sup> and Jacques Magnaudet<sup>2,†</sup>

<sup>1</sup>*IFP Energies Nouvelles, 69360 Solaize, France*

<sup>2</sup>*Institut de Mécanique des Fluides de Toulouse (IMFT), Université de Toulouse, CNRS, 31400 Toulouse, France*

Using fully-resolved simulations, we examine the torque experienced by a finite-length circular cylinder rotating steadily perpendicularly to its symmetry axis. The aspect ratio  $\chi$ , i.e., the ratio of the length of the cylinder to its diameter, is varied from 1 to 15. In the creeping-flow regime, we employ the slender-body theory to derive the expression of the torque up to order 4 with respect to the small parameter  $1/\ln(2\chi)$ . Numerical results agree well with the corresponding predictions for  $\chi \gtrsim 3$ . We introduce an *ad hoc* modification in the theoretical prediction to fit the numerical results obtained with shorter cylinders, and a second modification to account for the increase of the torque resulting from finite inertial effects. In strongly inertial regimes, a prominent wake pattern made of two pairs of counter-rotating vortices takes place. Nevertheless the flow remains stationary and exhibits two distinct symmetries, one of which implies that the contributions to the torque arising from the two cylinder ends are identical. We build separate empirical formulas for the contributions of pressure and viscous stress to the torque provided by the lateral surface and the cylinder ends. We show that, in each contribution, the dominant scaling law may be inferred from simple physical arguments. This approach eventually results in an empirical formula for the rotation-induced torque valid throughout the range of inertial regimes and aspect ratios considered in the simulations.

DOI: [10.1103/PhysRevFluids.6.094303](https://doi.org/10.1103/PhysRevFluids.6.094303)

## I. INTRODUCTION

Fibers and cylindrical rodlike particles are involved in numerous industrial processes such as paper making and food processing. In the chemical engineering industry, cylindrical pellets are used for instance for biomass extraction and oil refinement. Ice crystals growing and sedimenting in clouds also exhibit slender shapes and may be considered, to a first approximation, as cylindrical rods. Hydrodynamic forces and torques acting on slender cylindrical particles generally depend critically on their orientation with respect to the relative incoming flow, which greatly complicates their prediction. For instance, in the creeping-flow approximation, the hydrodynamic force acting on a long isolated fiber moving broadside on is known to be twice as large as the force it experiences when moving along its axis [1]. This anisotropic behavior may have critical consequences in industrial processes in which pressure losses have to be reduced to a minimum. It is thus of primary importance to predict accurately the instantaneous orientation of the particles, and consequently the hydrodynamic torque acting on them. For an isolated particle sedimenting in a fluid at rest in a regime in which inertial effects in the fluid are small, the time rate of change of the angular

\*[jean-lou.pierson@ifpen.fr](mailto:jean-lou.pierson@ifpen.fr)

†[magnau@imft.fr](mailto:magnau@imft.fr)

velocity is in most cases sufficiently weak for the rotation-induced torque to almost balance the inertial torque due to the body inclination [2]. Similarly, the rotation rate of small neutrally buoyant particles immersed in a linear flow is known to result from the approximate balance between the rotation-induced and the shear-induced torques [3], with possible inertial corrections in the latter [4,5]. This quasisteady approximation [6], together with the asymptotic expressions for the various contributions to the torque valid in the creeping-flow or low-but-finite-inertia regimes, have proven accurate for predicting the motion of small fibers settling in a vortical flow [7] or in a fluid at rest at infinity [8]. Since the pioneering work of [9], the same framework has also been used in simulations aimed at determining the statistical features of the orientation of fibers in turbulence, still assuming that the Reynolds number based on their diameter is much smaller than unity (see [10,11] for more recent references). However, under more general conditions, a proper prediction of the angular velocity, hence of the instantaneous body orientation, requires the influence of inertial effects on the rotation-induced torque to be accurately quantified for an arbitrary Reynolds number. With the aim of contributing to the modeling of the hydrodynamic torque under general flow conditions, the present paper focuses on the torque acting on an isolated finite-length circular cylinder rotating perpendicularly to its symmetry axis, from creeping-flow conditions to strongly inertial regimes. Indeed, the size of fibers encountered in applications covers a broad range corresponding to widely different flow regimes. While those employed in paper making industry have diameters typically in the range 15–30  $\mu\text{m}$  and are a few millimeters long, typical rodlike catalysts involved in fluidized beds have diameters of roughly 1 mm and are 5 to 10 mm long. In the former case, the Reynolds number based on the particle diameter is usually small, but the length-to-diameter aspect ratio is large. Conversely, flow conditions relevant to rod-like catalysts usually correspond to moderate-to-large diameter-based Reynolds numbers and aspect ratios of a few units. The problem addressed here is also directly relevant to the prediction of the flow structure induced by a rotating cylindrical rod driven by an electric or a magnetic field. This mixing technique is widely used in microfluidic devices [12] as well as in large stirred-tank reactors in which inertial effects dominate the induced flow [13]. In such devices, the actual shape of the rotating stirrer is usually more complicated than the one considered here, but results obtained with a cylindrical rod are expected to provide a first approximation of the rotation-induced torque and the flow structure far from the stirrer.

Although a large body of literature is available regarding the forces experienced by nonspherical particles (see, for instance, [14] for a review), much less is known regarding the torque, especially that resulting from the particle rotation. In the creeping-flow limit, Batchelor [1] made use of the slender-body theory to evaluate the force and torque acting on long cylindrical bodies. To the best of our knowledge, finite-Reynolds-number corrections to this prediction have not been derived so far. In the high-Reynolds regime, Kry and List [15,16] considered the torque experienced by rotating oblate spheroids. They employed a quasistatic approximation (different from the one mentioned above for the low-Reynolds-number regime) in which the instantaneous aerodynamic force and torque only depend on the flow Reynolds number and angular position of the particle with respect to the upstream flow at the same instant of time, but not on the particle angular velocity. They showed that this approximation is valid provided angular velocities are at least one order of magnitude less than the velocity of the incoming flow divided by the body characteristic length. They also pointed out that, under such conditions, a spinning motion about the spheroid minor axis modifies the boundary layer but does not affect significantly the pressure distribution about the body.

In this work, we determine numerically the torque experienced by a steadily rotating circular cylinder of finite length, from creeping-flow conditions to strongly inertial regimes. We briefly present the problem and the computational strategy in Sec. II. In Sec. III we first compute the torque in the low-Reynolds regime and compare the numerical results with the prediction of the slender-body approximation, which we extend to fourth order in Appendix A. Then we examine the influence of finite inertial effects and incorporate an empirical correction in the creeping-flow formula to take this influence into account. Moderate-to-large Reynolds number flow conditions are examined in Sec. IV. In the spirit of a recent investigation on the loads acting on an inclined

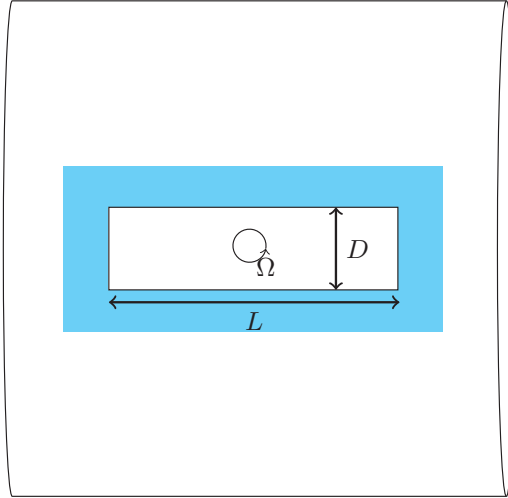


FIG. 1. Sketch of the computational domain (not to scale). The cyan area represents the region over which the grid is uniform.

translating cylinder [17], practical estimates for the torque acting on the body are derived from the simulations by considering separately the contribution of viscous stresses and pressure on each part of the body, i.e., the lateral surface and the two flat ends. We summarize our results in Sec. V and discuss qualitatively their implications with respect to the variations of the body rotation rate with the aspect ratio and the Reynolds number.

## II. PROBLEM DEFINITION AND NUMERICAL APPROACH

We consider the flow induced by a circular cylinder of length  $L$  and diameter  $D$  rotating about an axis perpendicular to its symmetry axis and passing through its center of inertia. The fluid is Newtonian, with density  $\rho$  and dynamic viscosity  $\mu$ , and is at rest at infinity. The problem depends on two dimensionless parameters, the aspect ratio  $\chi = L/D$  and the Reynolds number which we define as  $\text{Re} = \rho\Omega LD/(2\mu)$ . This definition assumes that  $D$  is the relevant length scale of the flow, while the characteristic velocity  $U$  is assumed to be  $\Omega L/2$ . In what follows, we investigate the flow and torque induced by the cylinder rotation in the range  $0.05 \leq \text{Re} \leq 240$  and  $1 \leq \chi \leq 15$ . In inertia-dominated regimes, we consider only aspect ratios in the range  $2 \leq \chi \leq 8$  to reduce the computational cost.

The computational strategy is based on the formulation introduced by Mougin and Magnaudet [18], and we refer to the original article for details. In short, the Navier-Stokes equations are solved for the *absolute* velocity field  $\mathbf{u}$  (the one measured by a fixed observer) using a coordinate system rotating and possibly translating with the body. Hence, the body and the grid rotate together (which avoids the need to regenerate the grid at each time step), while the fluid is at rest far away from the body. Note that this formulation differs from the classical one involving the Coriolis pseudoforce, since the latter makes use of the same coordinate system but considers the *relative* velocity field. In the present approach, the fluid obeys the no-slip condition  $\mathbf{u} = \boldsymbol{\Omega} \times \mathbf{x}$  at the cylinder surface,  $\mathbf{x}$  denoting the local position from the body centroid, and is at rest at infinity ( $\|\mathbf{u}\| \rightarrow 0$  for  $\|\mathbf{x}\| \rightarrow \infty$ ).

The computational domain is a large cylinder with the same axis as the body (Fig. 1). Its diameter is equal to its length. The discretization of the fluid domain is mostly similar to that used by Kharrouba *et al.* [17] but the configuration of interest here introduces some specificities. For low-to-moderate Reynolds numbers, the grid is uniform throughout the fluid region extending up

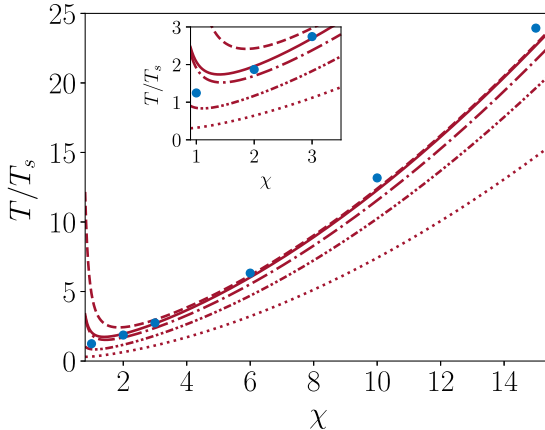


FIG. 2. Low-Reynolds-number torque on a rotating finite-length cylinder ( $T$ ), normalized by the torque on a rotating sphere with the same volume ( $T_s$ ), as a function of the aspect ratio  $\chi$ . Dotted, dash-dotted-dotted, dash-dotted, and dashed lines: predictions of first-, second-, third-, and fourth-order slender-body approximations, respectively; solid line: semiempirical formula (1),  $\bullet$ : numerical results for  $\text{Re} = 0.05$ . The region  $\chi \lesssim 3$  is magnified in the inset to clarify the behavior of the various approximations for short cylinders.

to  $0.5D$  from the body surface (blue region in Fig. 1), with cell sizes ranging from  $D/16$  to  $D/20$  depending on  $\text{Re}$ . Beyond this region, the cell size increases with the distance to the body following a geometric law with a common ratio close to 1.07. 32 cells are uniformly distributed in the azimuthal direction. The length and diameter of the domain range from  $60D$  for  $\chi = 1$  and 2 to  $215D$  for  $\chi = 10$  and 15. Such large dimensions are required due to the slow decrease of the disturbance induced by the body rotation. On the outer surface of the domain, the normal component of  $\mathbf{u}$  is assumed to be zero, together with the normal derivative of the tangential components. We select this “free-slip” condition rather than a nonreflecting outlet condition because the actual remaining velocity disturbance has an inward component on some parts of the outer surface, which could create numerical instabilities. In the inertia-dominated regime, detailed tests showed that the boundary layer, whose thickness is estimated to be  $\delta \sim D/\text{Re}^{1/2}$  on the body ends and on the part of the lateral surface close to them, is accurately captured with 6 cells. Hence, the cell size in the fluid region extending up to  $0.5D$  from the body surface is set to  $\delta/6$ . Here 64 cells are uniformly distributed in the azimuthal direction. The domain size is set to  $L + 30D$ , i.e., the outer boundary is located  $15D$  apart from the cylinder ends. Since the velocity disturbance decays faster with the distance to the body than in the low-to-moderate  $\text{Re}$  regime, a nonreflecting boundary condition [19] is used on the outer boundary.

### III. FROM THE CREEPING-FLOW REGIME TO MODERATE REYNOLDS NUMBERS

For  $\text{Re} = 0$ , the slender-body theory provides a convenient framework to estimate the torque on a rotating finite-length cylinder as long as the aspect ratio is much larger than unity. Batchelor [1] carried out the third-order expansion with respect to the small parameter  $\epsilon = 1/\ln(2\chi)$  for this case, computing the corresponding coefficients numerically. In Appendix A we derive these coefficients analytically up to order 4, based on the iterative technique developed by Keller and Rubinow [20].

The corresponding results are displayed in Fig. 2. The torque is made dimensionless by dividing it by its counterpart on a rotating sphere with the same volume, namely,  $T_s = -\pi\mu\Omega D^3$ , with  $D = (\frac{3}{2}\chi)^{1/3}D$ . The torque on a rotating cylinder is larger than that on the equivalent sphere for all aspect ratios  $\chi \gtrsim 1$ . Indeed, at leading order, the ratio of the two torques varies as  $\chi^2/\log(2\chi)$ . Not surprisingly, the first- and second-order approximations do not match the numerical results

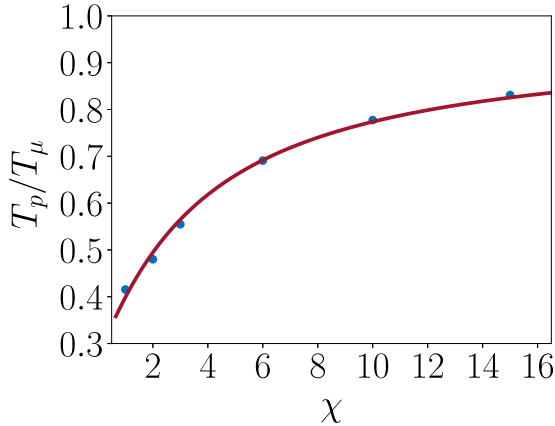


FIG. 3. Ratio of the pressure ( $T_p$ ) to the shear stress ( $T_\mu$ ) contributions to the torque for  $\text{Re} = 0.05$ . Solid line: empirical formula (2),  $\bullet$ : numerical results.

well, even for large aspect ratios. The third-order approximation provides a better estimate but still underpredicts the actual torque. A significantly better agreement is obtained with the fourth-order approximation for  $\chi \geq 3$ . All approximations diverge as  $\chi \rightarrow 1/2$ , making the agreement deteriorate for  $\chi \lesssim 3$ . However, the third-order approximation is still accurate in the range  $1.5 \lesssim \chi \lesssim 3$ . Making use of these observations, we introduce an *ad hoc* modification of the original expansion. That is, we multiply the fourth-order term by a function of  $\chi$  that quickly tends towards unity as  $\chi$  increases and towards zero when  $\chi \rightarrow 1/2$ , and varies in such a way that the behavior of the third-order expansion is recovered in the range  $2 \lesssim \chi \lesssim 3$ . The full expression reads

$$\begin{aligned}
 T = & -\frac{\pi\mu\Omega L^3}{3} \left\{ \epsilon + \epsilon^2 \left( \frac{11}{6} - \ln 2 \right) + \epsilon^3 \left( \frac{161}{36} - \frac{\pi^2}{12} - \frac{11}{3} \ln 2 + (\ln 2)^2 \right) \right. \\
 & + \epsilon^4 \left( 1 - \frac{1}{(2\chi)^{1.2}} \right)^5 \left[ -\frac{5}{4} \zeta(3) + \frac{1033}{72} - \ln^3(2) + \frac{11}{2} \ln^2(2) \right. \\
 & \left. \left. - \frac{161}{12} \ln 2 - \pi^2 \left( \frac{11}{24} - \frac{1}{8} \ln(4) \right) \right] \right\}, \tag{1}
 \end{aligned}$$

where the  $(2\chi)^{-1.2}$ -alteration of the prefactor of the  $O(\epsilon^4)$ -term is empirical. The formula (1) agrees well with the numerical results for  $\chi \gtrsim 2$ . It slightly deviates from the numerical result for  $\chi \geq 10$ . This is not unlikely since the Reynolds number based on  $L$  instead of  $D$  is of  $O(1)$  in this case, suggesting that inertial effects are already significant. The inset in Fig. 2 indicates that the normalized torque on a cylinder with  $\chi = 1$  is approximately 1.25, i.e., the torque is larger than that on the equivalent sphere,  $|T_s| \approx 1.145\pi\mu D^3\Omega$ . In Appendix B, we show how bounds for the torque may be derived from the minimum dissipation theorem. For  $\chi = 1$ , these predictions indicate that the torque is such that  $\pi\mu D^3\Omega \leq |T| \leq 2^{3/2}\pi\mu D^3\Omega$ . The numerical result obviously stands in the allowed interval.

Figure 3 shows how the ratio  $T_p/T_\mu$  between the pressure and shear stress contributions to the torque vary with the aspect ratio. The former contribution is observed to be smaller than the latter whatever  $\chi$ . Keeping in mind that  $T_p$  would be zero for a sphere, it is no surprise that  $T_p/T_\mu$  increases with  $\chi$ . This ratio is slightly larger than 0.8 for  $\chi = 15$ , and the observed variation suggests that it becomes independent of  $\chi$  and is of  $O(1)$  for long enough cylinders. Whatever the aspect ratio, the

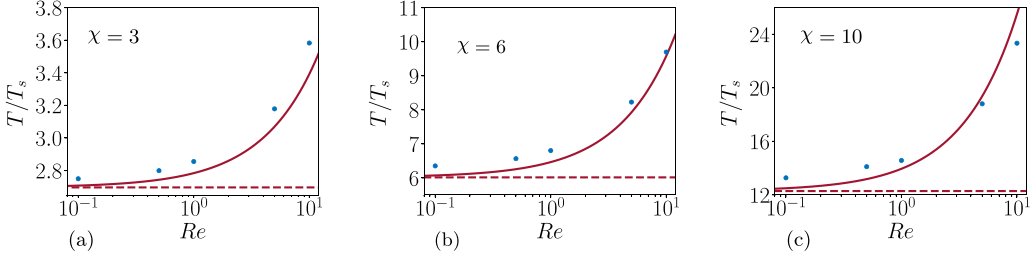


FIG. 4. Torque on a rotating finite-length cylinder ( $T$ ), normalized by the torque on a rotating sphere with the same volume ( $T_s$ ), as a function of the Reynolds number in the range  $0.1 \leq \text{Re} \leq 10$ .  $\bullet$ : numerical results; dashed line: creeping-flow prediction (1); solid line: semiempirical formula (3). The slight difference between numerical results and predictions of (1) for  $\text{Re} \ll 1$  is already present in Fig. 1 but is magnified here, owing to the chosen origin of the vertical axis.

numerical results are well fitted by the empirical formula

$$\frac{T_p}{T_\mu}(\text{Re} \approx 0) = 0.95 - \frac{2.7}{4 + 0.9\chi^{1.1}}. \quad (2)$$

Figure 4 displays the increase of the normalized torque as function of  $\text{Re}$  for three aspect ratios and Reynolds numbers up to 10. In the range  $0.05 \leq \text{Re} \leq 1$ , the torque is seen to vary by less than 5% for  $\chi = 3$ , while it varies by more than 10% for  $\chi = 10$ . For  $\text{Re} = 10$ , the torque on the longest cylinder has doubled with respect to its value in the creeping-flow regime, while it has only increased by nearly 40% for  $\chi = 3$ . That the relative contribution of inertial effects to the torque increases with the aspect ratio is no surprise. Indeed, the relevant characteristic length scale of the flow is the lever arm  $L/2 = \chi D/2$  rather than  $D$ , so that the relevant ratio of inertial to viscous effects is  $\frac{\chi}{2}\text{Re}$ . Finite inertial effects acting on a slender body inclined with respect to a uniform incoming flow were considered by Khayat and Cox [2], using the method of matched asymptotic expansions. Their predictions, in which inertial corrections affect the  $O(\epsilon^2)$ -terms of the expansion, quantify the inertia-induced increase of the drag and lift forces. In the case of a cylinder (more generally a body with a straight centerline), these predictions also reveal the existence of a nonzero inertial torque which tends to rotate the body broadside on with respect to the incoming flow. To the best of our knowledge, finite-inertia effects have not been considered for a slender body rotating in a fluid at rest at infinity. Adapting the approach of [2] to this configuration is beyond the scope of the present work. Instead, we only attempted to use the numerical results to extend the formula (1) empirically to  $O(1)$ -Reynolds numbers by suitably altering the prefactor of the  $O(\epsilon^2)$ -term. Based on the numerical findings and the above remarks, we modified (1) in the form

$$\begin{aligned} T = \frac{-\pi\mu\Omega L^3}{3} & \left\{ \epsilon + \epsilon^2 \left( \frac{11}{6} - \ln 2 + f(\chi, \text{Re}) \right) + \epsilon^3 \left( \frac{161}{36} - \frac{\pi^2}{12} - \frac{11}{3} \ln 2 + (\ln 2)^2 \right) \right. \\ & + \epsilon^4 \left( 1 - \frac{1}{(2\chi)^{1.2}} \right)^5 \left[ -\frac{5}{4} \zeta(3) + \frac{1033}{72} - \ln^3(2) + \frac{11}{2} \ln^2(2) \right. \\ & \left. \left. - \frac{161}{12} \ln 2 - \pi^2 \left( \frac{11}{24} - \frac{1}{4} \ln 2 \right) \right] \right\}, \quad (3) \end{aligned}$$

with  $f(\chi, \text{Re}) = 0.0337\chi^{1.3}\text{Re}^{0.9}$ . We left the pre-factors of the  $O(\epsilon^3)$  and  $O(\epsilon^4)$  contributions unaltered since, according to Fig. 4, the above change appears to be sufficient to capture most of the finite- $\text{Re}$  variations of the torque up to  $\text{Re} = 10$ . Note that given the definition of  $\text{Re}$ , the inertial correction to the torque provided by (3) behaves as  $\Omega^{1.9}$ , close to the theoretical  $\Omega^2$ -scaling expected on the basis of an Oseen-like asymptotic expansion [6].



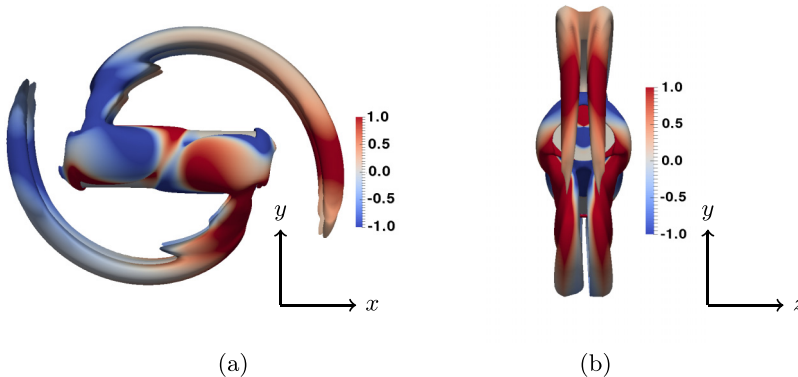


FIG. 5. Wake past a rotating cylinder with  $\chi = 3$  for  $\text{Re} = 220$ . (a) Side view from a fixed  $z$ -plane (see Fig. 6 for the exact definition of the coordinate system); (b) front view from a fixed  $x$ -plane. The wake is visualized using the  $Q$ -criterion [21]. The 0.001 isosurface of  $Q$  is colored with the magnitude of the normalized transverse vorticity  $\omega_z/\Omega$ .

#### IV. FLOW STRUCTURE AND TORQUE IN INERTIA-DOMINATED REGIMES

Inertia-dominated regimes with Reynolds numbers beyond those considered before are characterized by the presence of a prominent wake. The wake is visualized using the  $Q$ -criterion [21], where  $Q$  is the second invariant of the velocity gradient tensor, i.e.,  $Q = \frac{1}{2}(e_{ij}e_{ij} - \omega_{ij}\omega_{ij})$ , with  $e_{ij} = 1/2(\partial u_i/\partial x_j + \partial u_j/\partial x_i)$  and  $\omega_{ij} = 1/2(\partial u_i/\partial x_j - \partial u_j/\partial x_i)$  the components of the strain-rate and rotation-rate tensors, respectively. As Fig. 5 shows, two pairs of counter-rotating vortices take place. Each pair emanates from one end of the cylinder and roughly follows a circular path corresponding to the primary motion of fluid elements imposed by the body rotation. However, these fluid elements are also seen to move radially outward as they are advected downstream within each vortex (otherwise, each pair would hit the cylinder end opposite to the one it emanates from). This radial motion is due to the centrifugal force,  $\mathbf{F}_c$ . In the reference frame rotating with the cylinder, this force reads  $\mathbf{F}_c = -\boldsymbol{\Omega} \times (\boldsymbol{\Omega} \times \mathbf{x}) = \Omega^2 r_{\perp} \mathbf{e}_{\perp}$ , with  $\mathbf{e}_{\perp}$  the unit vector collinear to the projection of  $\mathbf{x}$  onto the plane perpendicular to  $\boldsymbol{\Omega}$ , and  $r_{\perp} = \|\mathbf{x} \times \boldsymbol{\Omega}\|/\Omega = (x^2 + y^2)^{1/2}$  the radial position of a fluid element in that plane, measured from the rotation axis. This centrifugal force makes the radial velocity component  $u_{\perp} = \mathbf{u} \cdot \mathbf{e}_{\perp}$  increase along the path of a fluid element, yielding the observed increase in the radial position of a vortex thread as the downstream distance to its origin increases. Since the magnitude of the vorticity generated at the cylinder surface increases with  $\text{Re}$ , so does the strength of the vortices. No unsteadiness, i.e., no vortex shedding, was observed throughout the whole range of Reynolds number considered here ( $\text{Re} \leq 240$ ). In this respect, the present wake structure is similar to that observed past a fixed sphere in between the first and second bifurcations [22], an intermediate stationary but nonaxisymmetric regime in which the wake is made of two counter-rotating vortex threads where streamwise vorticity is concentrated. The present wake exhibits two distinct symmetries. As Fig. 5(b) reveals, the plane perpendicular to the rotation axis and passing through the cylinder centroid is a symmetry plane. This planar symmetry, combined with the flow steadiness, implies that all force components are zero at any instant of time and that the torque is collinear with the rotation axis.

Figure 5(a) reveals a second symmetry resulting from the combination of two mirror symmetries. One is with respect to the plane containing both the rotation axis and the cylinder symmetry axis (defined as the  $z$ - and  $x$ -axes in Fig. 6, respectively). The other is with respect to the plane orthogonal to the previous plane and containing again the rotation axis [ $(y, z)$ -plane in Fig. 6]. This symmetry is illustrated with colored areas in Fig. 6. For instance, the pressure at a given point in the upper half of the right end (blue area) is identical to the pressure at the mirror point of the left end (blue area

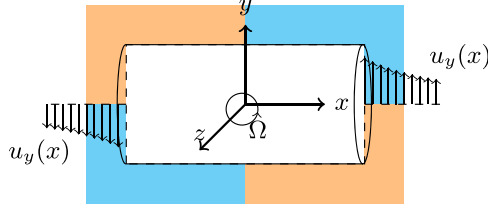


FIG. 6. Sketch of the flow configuration near the rotating cylinder, especially the distribution of  $u_y$  (the  $y$ -component of the fluid velocity) close to the ends. Colors help identify the flow symmetries.

again). Since the cross product  $\mathbf{x} \times \mathbf{n}$  (with  $\mathbf{n}$  the unit normal to the cylinder pointing into the fluid) is also the same at both locations, it turns out that the pressure contributions to the torque provided by the two ends are identical. The  $x$ -variation of the tangential velocity  $u_y$  in the vicinity of both ends is schematized in Fig. 6. As this sketch suggests, the same property holds true for the shear stress contribution provided by both ends.

Figure 7 displays the contributions to the torque arising from the lateral surface. For  $\chi = 8$ , computations were carried out only up to  $Re = 60$ , owing to the cost associated with the large grids required to capture the flow details at higher  $Re$ . From now on, we characterize the torque through the coefficient  $C_T$  obtained by normalizing  $T$  with the reference torque  $\frac{1}{8}\rho\Omega^2L^4D$ , since the characteristic velocity is  $\Omega L/2$  and the characteristic area is  $LD$ . For each aspect ratio, the viscous contribution [Fig. 7(a)] decreases approximatively as  $Re^{-1/2}$ , indicating that the magnitude of the shear stress is dictated by the boundary layer thickness. This contribution is also seen to depend only weakly on  $\chi$  as soon as  $\chi \gtrsim 5$ . Hence, the corresponding coefficient can be fitted with the simple expression

$$C_{T\mu l} = (1.32\chi^{-2} + 0.55)Re^{-1/2}. \quad (4)$$

The pressure contribution [Fig. 7(b)] decreases as  $\chi$  or  $Re$  increases, gradually tending toward a constant value for large Reynolds numbers whatever  $\chi$ . Numerical data are properly fitted with the three-term correlation

$$C_{Tpl} = 1.21\chi^{-0.23}Re^{-0.75} + 0.12\chi^{-2} + 0.1. \quad (5)$$

This fit suggests that the pressure contribution to the torque tends toward 0.1 for large enough Reynolds numbers and infinitely long cylinders. Although a torque coefficient independent of both  $\chi$  and  $Re$  is to be expected in this limit, it must be kept in mind that only the steady regime is considered here, so that (5) may not be valid in the unsteady regimes that take place for sufficiently

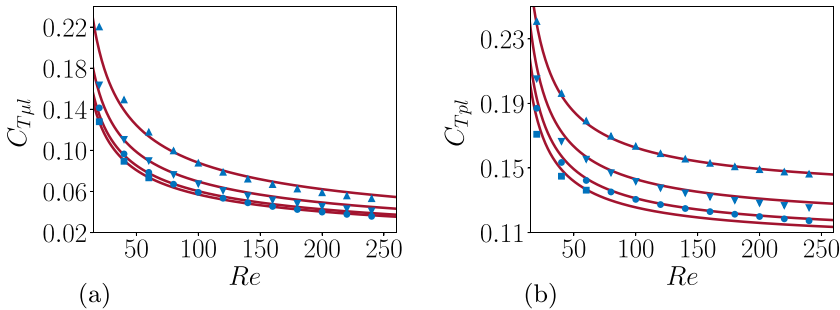


FIG. 7. Contributions to the torque coefficient arising from the lateral surface as a function of  $Re$ . (a) Shear-induced viscous contribution ( $C_{T\mu l}$ ); (b) pressure contribution ( $C_{Tpl}$ ).  $\blacktriangle$ :  $\chi = 2$ ,  $\blacktriangledown$ :  $\chi = 3$ ,  $\bullet$ :  $\chi = 5$ ,  $\blacksquare$ :  $\chi = 8$ . Solid line: empirical fits (4) and (5).

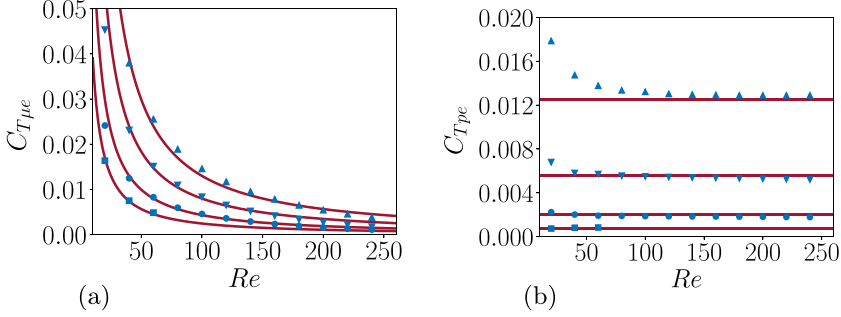


FIG. 8. Contributions to the torque coefficient arising from each of the cylinder ends as a function of  $Re$ . (a) Shear-induced viscous contribution ( $C_{T_{\mu e}}$ ); (b) pressure contribution ( $C_{T_{pe}}$ ).  $\blacktriangle$ :  $\chi = 2$ ,  $\blacktriangledown$ :  $\chi = 3$ ,  $\bullet$ :  $\chi = 5$ ,  $\blacksquare$ :  $\chi = 8$ . Solid line: empirical fits (6) and (7).

large  $Re$ . Figure 8 displays the contribution of each cylinder end to the torque. The viscous contribution [Fig. 8(a)] decreases strongly as  $\chi$  or  $Re$  increases. It is adequately fitted with the simple formula

$$C_{T_{\mu e}} = 7.5\chi^{-1.2}Re^{-1.2}. \quad (6)$$

It is worth noting that the negative  $Re$  exponent is significantly higher than the  $-1/2$  exponent provided by the boundary layer scaling [23]. The reason is that the flow is massively separated in the end regions, and the typical length scale of the corresponding recirculation is  $D$ . For this reason, the magnitude of the shear stress on the cylinder ends is governed by the cylinder diameter, not by the boundary layer thickness. This scaling yields viscous stresses of  $O(\mu U/D)$ , hence contributions to the torque of  $O(\mu ULD)$ , which results in  $C_{T_{\mu e}} \sim Re^{-1}\chi^{-1}$ , close to the behavior synthesized by (6).

As Fig. 8(b) reveals, the pressure contribution to the torque arising from the cylinder ends does not vary significantly with the Reynolds number in the range of interest here, except for the shortest cylinder for which some decrease is observed for  $Re \leq 80$ . Compared to the pressure contribution provided by the lateral surface,  $C_{T_{pe}}$  is one order of magnitude smaller for  $\chi = 2$  and approximately 50 times smaller for  $\chi = 5$ . This small contribution is seen to decrease strongly with the aspect ratio. This decrease may readily be predicted, assuming that the pressure on the ends scales as  $\rho U^2 \sim \rho \Omega^2 L^2$ . Since the end area is of  $O(D^2)$  and the magnitude of  $\mathbf{x} \times \mathbf{n}$  is of  $O(D)$  there, the pressure contribution to the torque scales as  $\rho \Omega^2 L^2 D^3$ , which yields  $C_{T_{pe}} \sim \chi^{-2}$ . Indeed, the behaviors reported in Fig. 8(b) are adequately fitted by the simple expression

$$C_{T_{pe}} = 0.05\chi^{-2}. \quad (7)$$

The total torque coefficient  $C_T$  is eventually obtained by summing all the contributions fitted in (4)–(7), keeping in mind that those of (6) and (7) have to be counted twice. This yields

$$C_T(\chi, Re) = 15\chi^{-1.2}Re^{-1.2} + 1.21\chi^{-0.23}Re^{-0.75} + (1.32\chi^{-2} + 0.55)Re^{-1/2} + 0.22\chi^{-2} + 0.1. \quad (8)$$

As Fig. 9 shows, this empirical fit matches all numerical results well.

The ratio of the pressure contribution ( $T_p$ ) to the viscous contribution ( $T_\mu$ ) to the torque may also be computed from (4)–(7). Using these estimates, one finds

$$\frac{T_p}{T_\mu} = \frac{1.21\chi^{-0.23}Re^{-0.75} + 0.1 + 0.22\chi^{-2}}{(1.32\chi^{-2} + 15\chi^{-1.2} + 0.55)Re^{-1/2}}. \quad (9)$$

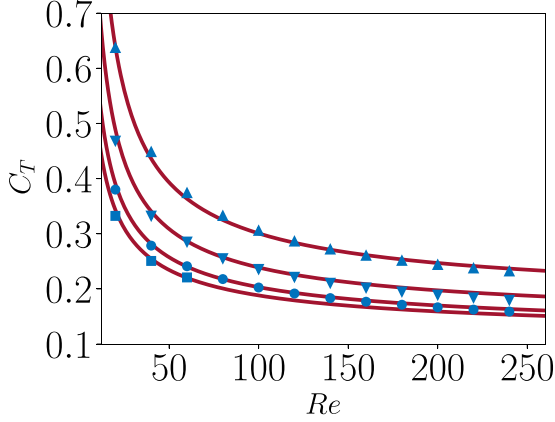


FIG. 9. Torque coefficient ( $C_T$ ) as a function of  $Re$  for cylinders with various aspect ratios.  $\blacktriangle$ :  $\chi = 2$ ,  $\blacktriangledown$ :  $\chi = 3$ ,  $\bullet$ :  $\chi = 5$ ,  $\blacksquare$ :  $\chi = 8$ . Solid line: empirical fit (8).

For sufficiently large aspect ratios and Reynolds numbers, this ratio tends toward  $0.18Re^{1/2}$ . Thus it becomes independent of  $\chi$  and increases as the square root of the Reynolds number, boundary layer effects making the viscous contribution decrease as  $Re^{-1/2}$ . These features are confirmed in Fig. 10, which displays  $T_p/T_\mu$  as a function of  $\chi$  for various  $Re$ . Remarkably, variations of this ratio with respect to  $\chi$  are qualitatively similar to those observed in the low-Reynolds-number regime (see Fig. 3). The slight deviation of (9) from the numerical data for  $Re = 240$  results from the fact that (4) somewhat overestimates the shear stress contribution at large Reynolds number, as may be discerned in Fig. 7.

## V. DISCUSSION

In this work, we used fully resolved simulations to obtain approximate laws for the torque acting on a slender circular cylinder rotating about an axis passing through its centroid and perpendicular to its symmetry axis. For cylinders with an aspect ratio larger than 3, we found

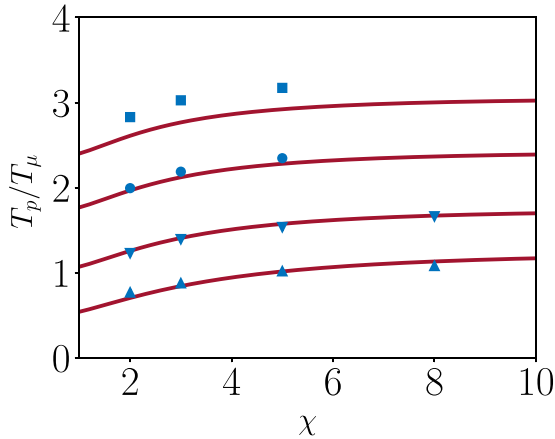


FIG. 10. Ratio of the pressure ( $T_p$ ) to shear stress ( $T_\mu$ ) contributions to the torque as a function of the cylinder aspect ratio for different Reynolds numbers.  $\blacktriangle$ :  $Re = 20$ ,  $\blacktriangledown$ :  $Re = 60$ ,  $\bullet$ :  $Re = 140$ ,  $\blacksquare$ :  $Re = 240$ ; solid line: empirical formula (9).

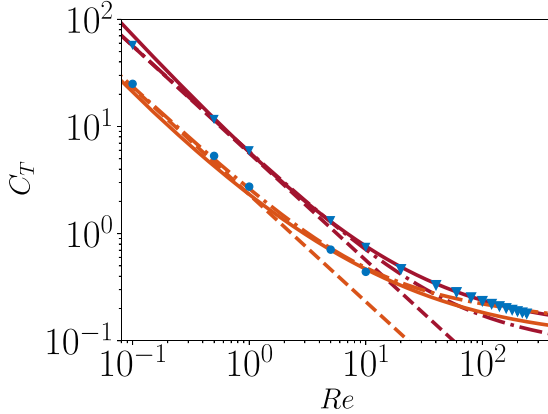


FIG. 11. Torque coefficient ( $C_T$ ) as a function of  $Re$  for cylinders with various aspect ratios. Numerical results for:  $\chi = 3$  ( $\blacktriangledown$ ) and  $\chi = 10$  ( $\bullet$ ). Dashed line: creeping-flow prediction (1); dash-dotted line: finite- $Re$  semiempirical formula (3); solid line: empirical inertial fit (8); red and orange lines refer to  $\chi = 3$  and  $\chi = 10$ , respectively.

the creeping-flow prediction based on the slender-body theory to agree well with numerical data, provided the expansion with respect to the small parameter  $1/\ln(2\chi)$  is carried out up to fourth order. We empirically modified the fourth-order term which we derived analytically, in such a way that the modified formula is valid down to  $\chi \approx 2$ . We carried out a series of runs in the range  $0.1 \leq Re \leq 10$  to quantify finite-inertia effects. As is customary with slender bodies, numerical results revealed that the larger the aspect ratio the stronger the inertial increase of the torque for a given  $Re$ . Since no theoretical prediction is available for low-but-finite inertial effects in the configuration considered here, we merely introduced an empirical modification in the second-order term of the low- $Re$  prediction to account for these effects. The modified formula was found to fit the numerical data well up to  $Re \approx 10$  whatever the aspect ratio. Then we considered higher Reynolds numbers, up to  $Re = 240$ . Numerical results revealed that the flow remains stationary throughout this range and preserves a planar symmetry with respect to the plane perpendicular to the rotation axis and passing through the body centroid. The flow exhibits a second symmetry, resulting from the combination of two mirror symmetries with respect to two mutually orthogonal planes. Because of this symmetry, the two cylinder ends provide identical contributions to the torque. We used numerical data to establish separate approximate fits for the contributions resulting from pressure and viscous effects on each part of the body surface, and provided simple physical arguments in support of the corresponding scaling laws. From a practical standpoint, the main outcomes of this investigation are formulas (1), (3), and (8), which accurately approach the rotation-induced torque from creeping-flow conditions up to  $Re \approx 250$  for all aspect ratios larger than 2.

These various predictions are displayed throughout the  $Re$ -range explored numerically in Fig. 11, together with the numerical results obtained for  $\chi = 3$  and 10. Remarkably, the empirical fit (8) derived in the inertia-dominated regime turns out to predict the torque well even for low-to-moderate Reynolds numbers, down to  $Re \approx 1$ . For lower  $Re$ , it overpredicts the torque for  $\chi = 3$  but under-predicts it for  $\chi = 10$ . It may also be noticed that the applicability of the semiempirical formula (3) remains limited to  $Re \approx 10$  for both aspect ratios. The semiempirical law (3) is potentially useful to estimate the rotation rate of sedimenting cylindrical rodlike particles and fibers in the low-but-finite Reynolds number regime. In that regime, the orientation-induced inertial torque  $T_o$  acting on a long nonrotating cylinder translating with velocity  $U$  in a fluid at rest is known to be of  $O(\mu UL^2 \chi Re_u / [\ln \chi]^2)$  [2], with  $Re_u$  the Reynolds number based on the body diameter and velocity  $U$  assumed to be small. In contrast, according to (3), the rotation-induced torque on a long nontranslating cylinder scales as  $T \sim \mu \Omega L^3 / \ln \chi$ , provided the inertial correction remains small. A

rodlike particle settling under the effect of gravity experiences both translation and rotation. In this case, the nonlinear coupling between the translation- and rotation-induced flows yields an additional inertial correction to the loads proportional to  $\Omega U$ , so that the total inertial contribution to the hydrodynamic force and torque is generally the sum of three terms proportional to  $U^2$ ,  $\Omega^2$ , and  $\Omega U$ , respectively, with distinct prefactors that depend on the body geometry [6]. The  $\Omega U$ -term is at the origin of the Magnus lift force acting on a spinning sphere translating perpendicularly to its rotation axis [24]; no inertial correction to the torque takes place at this order of approximation in this specific case. To the best of our knowledge, this correction has not been explicitly computed in the configuration considered here, i.e., a cylinder that settles in a vertical plane containing its symmetry axis and rotates about an axis perpendicular to this plane. However this inertial correction is presumably significantly smaller than  $T_o$  as far as  $L\Omega U$  remains small compared to  $U^2$ , i.e.,  $\Omega L/U \ll 1$ . Assuming that this is the case and the time rate-of-change of the particle angular momentum is also small compared to  $T_o$  (see [6] for a discussion on this aspect), the angular velocity of a long cylinder with uniform density settling under conditions  $\text{Re}_u \ll 1$  and  $\text{Re} \ll 1$  must be such that  $T$  and  $T_o$  almost balance each other. This quasisteady balance implies

$$\frac{\Omega L}{U} \sim \text{Re}_u \frac{\chi}{\ln \chi}. \quad (10)$$

The settling velocity is readily estimated by requesting that the drag force, which in this regime scales as  $F_d \sim \mu U L / (\ln \chi)$  irrespective of the cylinder orientation [1], balances the net weight of the body,  $F_g$ . This constraint yields  $\text{Re}_u \sim (\rho F_g / \mu^2) \chi^{-1} \ln \chi \equiv \text{Ar}^2 \chi^{-1} \ln \chi$ , where  $\text{Ar} = (\rho F_g)^{1/2} / \mu$  is the Archimedes number characterizing the relative strength of gravitational (hence inertial) effects and viscous effects during the body settling. Injecting the above estimate for  $\text{Re}_u$  into (10) results in

$$\frac{\Omega L}{U} \sim \text{Ar}^2. \quad (11)$$

Hence, the magnitude of  $\Omega L/U$  is found to be small provided  $\text{Ar}$  is small, in line with the above assumption. The same qualitative reasoning may be applied to moderately inertial regimes (i.e., typically  $\text{Re}$  and  $\text{Re}_u$  in the range 1–10), assuming that although cross-effects between rotation and translation certainly contribute quantitatively to the hydrodynamic torque, they remain small enough to leave the scaling of the leading-order contributions unchanged. Numerical predictions for the force and torque acting on an inclined translating (but nonrotating) cylinder were recently obtained over a wide range of  $\text{Re}_u$  in [17]. In this reference, similar to the approach followed in the previous section, the results for  $T_o$  in inertia-dominated regimes were synthesized in the form of an empirical fit. Considering that the cylinder axis makes an angle  $\theta$  with the translation velocity, and writing  $T_o$  in the form  $T_o(\chi, \theta, \text{Re}_u) = C_{T_o}(\chi, \text{Re}_u) \rho U^2 L^2 D \sin 2\theta$ , these results show that  $C_{T_o} \approx 0.7 \chi^{-0.47} \text{Re}_u^{-0.35}$  in the limit of large aspect ratios. For  $\chi = 10$  and  $\text{Re} = O(1)$ , Fig. 11 indicates that  $C_T$  follows the approximate law  $C_T \approx 2.8 \text{Re}^{-0.83}$ .

Therefore, when  $\text{Re}$  is of  $O(1)$ , still assuming that cross-effects of  $\Omega$  and  $U$  are small enough for the zero-net torque condition to require the leading-order contributions to  $T$  and  $T_o$  to approximately balance each other,  $\Omega L/U$  obeys

$$\frac{\Omega L}{U} \approx 1.1 \left( \frac{\text{Re}_u}{\chi} \right)^{0.4}. \quad (12)$$

When the cylinder settles broadside on ( $\theta = 90^\circ$ ) and  $5 \lesssim \text{Re}_u \lesssim 10$ , the results of [17] indicate that the drag force is approximately  $F_d \approx 5.15 \text{Re}_u^{-0.55} L D \rho U^2$ . Hence, balancing  $F_d$  and  $F_g$  implies  $\text{Re}_u \approx 0.32 (\text{Ar}^2 / \chi)^{0.7}$  which, once injected into (12), yields

$$\frac{\Omega L}{U} \approx 0.7 \text{Ar}^{0.55} \chi^{-0.7}. \quad (13)$$

Similarly, when the cylinder settles along its axis ( $\theta = 0^\circ$ ), the drag force was found to scale approximately as  $F_d \approx 12.9 \text{Re}_u^{-0.8} \chi^{-0.3} LD\rho U^2$ , which changes (13) into

$$\frac{\Omega L}{U} \approx 0.5 (\text{Ar}/\chi)^{0.65}. \quad (14)$$

According to (13) and (14),  $\Omega L/U$  is small (i.e., the above approximate torque balance may be expected to be valid) provided  $\chi$  is somewhat larger than  $\text{Ar}$ . For instance, with  $\text{Ar} = 50$  and  $\chi = 50$ , which corresponds to  $\text{Re}_u \approx 5$ , these predictions suggest  $\Omega L/U \approx 0.4$  (hence  $\text{Re} \equiv \text{Re}_u \frac{\Omega L}{2U} \approx 1$ ) and  $\Omega L/U \approx 0.5$  ( $\text{Re} \approx 1.25$ ), respectively, so that  $\text{Re}$  is close to unity whatever the cylinder orientation. Doubling  $\chi$  while maintaining  $\text{Ar}$  unchanged reduces the relative rotation velocity to 0.25 and 0.30, respectively. Comparing (11) with (13) or (14) provides some qualitative insight into the way the relative rotation rate  $\Omega L/U$  varies with the Archimedes number and the body aspect ratio in the limit  $\chi \gg 1$ . Starting from the quadratic behavior indicated by (11) for low-but-finite Archimedes numbers, (13) and (14) predict that the growth of  $\Omega L/U$  with  $\text{Ar}$  strongly slows down for moderately inertial conditions. Also, while the aspect ratio is found to have no effect at leading order on the relative rotation rate when  $\text{Ar}$  is small, the larger  $\chi$  the slower  $\Omega L/U$  in the moderately inertial regime.

Throughout this work, we deliberately disregarded unsteady effects. Such effects are obviously significant, if not dominant, during collision processes [25]. Similarly, they can hardly be ignored in a turbulent flow during the stage a particle enters or leaves a vortical structure with significant size and energy. In such situations, the rotation-induced torque may be transiently significantly larger than the translation- or shear-induced components of the hydrodynamic torque, the torque balance then being satisfied thanks to the time rate of change of the particle angular momentum. In a suspension, the collision frequency increases with the particle concentration, making these transient effects become increasingly important as denser suspensions are concerned. In a turbulent flow, the paths of fluid and rigid particles become increasingly different as the particle size and the particle-to-fluid relative density difference increase, making the occurrence of strongly time-dependent events along the particle path more frequent. In such situations, accounting for the influence of time-dependent effects on the hydrodynamic torque and estimating the relaxation time beyond which quasisteady approximate formulas such as those established here become valid again is of primary importance. However, the history force on a rotating slender body (i.e., the counterpart of the Basset-Boussinesq force for a sphere) is not known in closed form, even in the Stokes regime. Similarly, in the inviscid limit, the inertia-induced (or added-mass) torque is not known in closed form, although approximate formulas have been proposed [26]. This lack of theoretical guides in the asymptotic regimes makes the development of approximate predictions for such unsteady situations challenging. However, given their practical relevance, there is a definite need to examine these transient effects in future studies.

## ACKNOWLEDGMENTS

M.K.'s fellowship was provided by IFP Energies Nouvelles, whose financial support is greatly appreciated. Part of the computations were carried out on the IRENE supercomputer under GENCI Grant No. A0072B10978. We acknowledge discussions with Prof. Ganesh Subramanian regarding the theoretical evaluation of inertial corrections to the rotation-induced torque.

## APPENDIX A: SLENDER-BODY APPROXIMATION FOR THE ROTATION-INDUCED TORQUE

The torque on a long rotating body may be obtained through the slender-body theory [1,20]. By expanding the solution in powers of the small parameter  $\epsilon = 1/\ln(2\chi)$ , Batchelor [1] determined the rotation-induced torque up to  $O(\epsilon^3)$ . The coefficients of the corresponding expansion were obtained numerically. However, the logarithmic dependence of the loads with respect to  $\chi$  makes the expansion converge slowly, limiting the accuracy of the predictions for moderate aspect ratios. This

is why including higher-order contributions is desirable. In this Appendix, we derive the coefficients of the  $\epsilon^n$ -expansion up to  $n = 4$ . The total torque on a cylindrical body of length  $L$  may be written as

$$\mathbf{T} = -8\pi\mu L^2 \int_0^1 \mathbf{x} \times \mathbf{f}(x) dx, \quad (\text{A1})$$

where  $\mathbf{f}(x)$  is the density of the Stokeslet distribution along the body,  $\mathbf{x}$  is the local position (with  $x = 1/2$  at the body centroid) and  $x$  denotes the arc length. For a body rotating along an axis perpendicular to its symmetry axis (here along  $z$  as in the main body of the paper), the previous expression reduces to

$$T = -8\pi\mu L^2 \int_0^1 x f_y(x) dx. \quad (\text{A2})$$

The Stokeslet density  $f_y$  was obtained by Keller and Rubinow [20], using a matched asymptotic expansion technique. It may be expressed as

$$f_y(x) = -\frac{\epsilon}{2} \left( U_y(x) + f_y(x) \{ \ln[4x(1-x)] + 1 \} + \int_{-x}^{1-x} \frac{f_y(x+t) - f_y(x)}{|t|} dt \right), \quad (\text{A3})$$

with  $U_y$  the rotation-induced velocity of the cylinder in the  $y$ -direction. For  $\chi \gg 1$ ,  $U_y = \Omega L(x - 1/2)$ , which indicates that the rotation-induced flow is equivalent to a uniform shear flow of strength  $\Omega$  centered at the body centroid. As detailed in [20],  $f_y(x)$  may be obtained in an iterative way. Setting first  $f_y(x) = 0$  on the right-hand side of (A3), the first-order approximation is obtained as  $f_y^{(1)}(x) = -\Omega L(x - 1/2)\epsilon/2$ . Inserting the first-order solution in the right-hand side of (A3), the second-order correction is readily obtained as

$$f_y^{(2)}(x) = -\frac{\Omega L(x - 1/2)}{2} \left( \epsilon - \frac{\epsilon^2}{2} \{ \ln[4x(1-x)] - 1 \} \right), \quad (\text{A4})$$

since the integral term in (A3) reduces to  $\int_{-x}^{1-x} \frac{t}{|t|} dt = 1 - 2x$ . Following the same procedure, one obtains the third-order correction in the form

$$f_y^{(3)}(x) = -\frac{\Omega L(x - 1/2)}{2} \left[ \epsilon - \frac{\epsilon^2}{2} \{ \ln[4x(1-x)] - 1 \} + \frac{\epsilon^3}{4} \left( \{ \ln[4x(1-x)] - 1 \} \{ \ln[4x(1-x)] + 1 \} + \frac{g_y^{(3)}(x)}{x - 1/2} \right) \right], \quad (\text{A5})$$

where  $g_y^{(3)}(x) = \int_{-x}^{1-x} [h_y^{(3)}(x+t) - h_y^{(3)}(t)]/|t| dt$ , with  $h_y^{(3)}(x) = (x - 1/2)\{ \ln[4x(1-x)] - 1 \}$ . The latter integral may be evaluated analytically, yielding

$$g_y^{(3)}(x) = -3 + \frac{\pi^2}{6} + 6x - \frac{\pi^2}{3}x + 6 \ln 2 - 12x \ln 2 + 2 \ln(1-x) - 2x \ln(1-x) - 2x \ln(x) + \left( \frac{1}{2} - x \right) \left[ \text{Li}_2 \left( \frac{x-1}{x} \right) + \text{Li}_2 \left( \frac{x}{x-1} \right) \right], \quad (\text{A6})$$

where  $\text{Li}_2$  is the polylogarithm function with argument 2. At this stage, the present prediction may be compared with the coefficients computed numerically by Batchelor [1]. For this purpose one needs the results

$$\int_0^1 x(x - 1/2) \{ \ln[4x(1-x)] - 1 \} dx = -11/36 + \ln 2/6,$$

$$\int_0^1 x(x - 1/2) \{ \ln[4x(1-x)] - 1 \} \{ \ln[4x(1-x)] + 1 \} dx = [95 - 3\pi^2]$$



$$+ 12 \ln 2(-8 + \ln 8)]/108,$$

$$\int_0^1 x g_y^{(3)}(x) dx = 11/18 - \ln 2/3.$$

The third-order approximation for the torque is then found to be

$$T^{(3)} = \frac{-\pi \mu \Omega L^3}{3} \left[ \epsilon + \epsilon^2 \left( \frac{11}{6} - \ln 2 \right) + \epsilon^3 \left( \frac{161}{36} - \frac{\pi^2}{12} - \frac{11}{3} \ln 2 + (\ln 2)^2 \right) \right]. \quad (\text{A7})$$

The numerical evaluation of the second- and third-order terms in (A7) agrees with the results provided in [1]. At next order, the Stokeslet density may be expressed as

$$f_y^4(x) = f_y^{(3)}(x) + \frac{\Omega L(x - 1/2)}{16} \epsilon^4 \left[ \{\ln[4x(1-x)] + 1\} \left( \{\ln[4x(1-x)] - 1\} \{\ln[4x(1-x)] + 1\} \right. \right. \\ \left. \left. + \frac{g_y^{(3)}(x)}{x - 1/2} \right) + \frac{g_y^{(4)}(x)}{x - 1/2} \right], \quad (\text{A8})$$

where  $g_y^{(4)}(x) = \int_{-x}^{1-x} [h_y^{(4)}(x+t) - h_y^{(4)}(t)]/|t| dt$  with  $h_y^{(4)}(x) = (x - 1/2) \{\ln[4x(1-x)] - 1\} \{\ln[4x(1-x)] + 1\} + g_y^{(3)}(x)$ . Integrating separately each contribution, one obtains

$$\int_0^1 x(x - 1/2) \{\ln[4x(1-x)] - 1\} \{\ln[4x(1-x)] + 1\}^2 dx \\ = \frac{1}{216} [216\zeta(3) - 1042 + 6 \ln 4 [85 + 3 \ln 4 (\ln 4 - 7)] + \pi^2 (42 - 9 \ln 16)], \\ \int_0^1 x g_y^{(3)} \{\ln[4x(1-x)] + 1\} dx = \frac{1}{54} [-9\zeta(3) - 95 + 3\pi^2 - 36 \ln^2(2) + 96 \ln 2], \\ \int_0^1 x g_y^{(4)} dx = \frac{1}{54} [-161 + 3\pi^2 - 9 \ln^2(4) + 54 (\ln 4 + \frac{4}{9} \ln 2)].$$

Summing all contributions, the fourth-order approximation is eventually obtained as

$$T^{(4)} = T^{(3)} - \frac{\pi \mu \Omega L^3 \epsilon^4}{3} \left[ -\frac{5}{4} \zeta(3) + \frac{1033}{72} - \ln^3(2) + \frac{11}{2} \ln^2(2) - \frac{161}{12} \ln 2 \right. \\ \left. - \pi^2 \left( \frac{11}{24} - \frac{1}{4} \ln 2 \right) \right], \quad (\text{A9})$$

where  $\zeta$  denotes the Riemann zeta function. Interestingly, at each order of the expansion one may remark that  $\int_0^1 x \int_{-x}^{1-x} [f_y(x+t) - f_y(x)]/|t| dt dx = -2 \int_0^1 x f_y(x) dx$ . This statement may presumably be proved by mathematical induction, even though we did not attempt to do so.

The Stokeslet distribution  $f_y(x)$  may be thought of as the transverse force per unit length acting on the cylinder at position  $x$ . Figure 12 shows how the first three orders of this force distribution vary along the cylinder axis [we did not obtain the function  $g_y^{(4)}(x)$  involved in (A8) in closed form and thus could not compute the distribution of  $f_y^4(x)$ ]. This figure makes it clear that, while the first-order distribution is linear, higher-order corrections peak more and more near the cylinder ends as the order increases, which was to be expected since these higher-order terms account for finite-length effects.

## APPENDIX B: MINIMUM DISSIPATION THEOREM FOR A ROTATING CYLINDER

The minimum dissipation theorem states that in any geometrical configuration, the Stokes solution dissipates less energy than any other solenoidal solution satisfying the same boundary conditions. For a translating and rotating rigid body, the dissipation rate may be related to the rate of work of the force and torque. Therefore [27,28]

$$\mathbf{F} \cdot \mathbf{U} + \mathbf{T} \cdot \boldsymbol{\Omega} \leq \Phi^*, \quad (\text{B1})$$

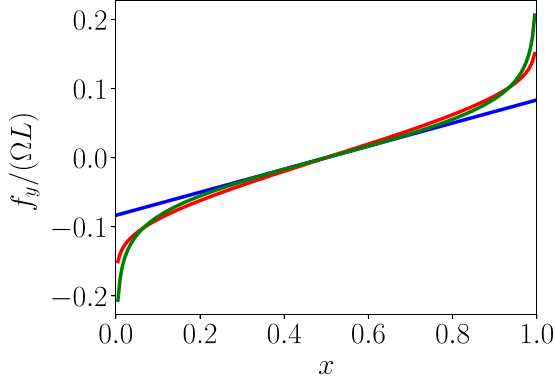


FIG. 12. Successive orders of the Stokeslet density distribution  $f_y(x)$  along the cylinder. The blue, red, and green lines correspond to  $f_y^1$ ,  $f_y^2$ , and  $f_y^3$ , respectively.

where  $\mathbf{F}$  and  $\mathbf{T}$  are the force and torque acting on the body moving at velocity  $\mathbf{U}$  and rotating with angular velocity  $\boldsymbol{\Omega}$ , and  $\Phi^*$  is the dissipation rate of any other solenoidal velocity field  $\mathbf{u}^*$  obeying the same boundary conditions. This theorem has been used successfully to estimate bounds for the drag acting on translating bodies [27]. The corollary for rotating bodies directly follows from (B1). Assuming that a rigid body bounded by a surface  $\mathcal{S}_i$  is immersed in a body of fluid bounded externally by a surface  $\mathcal{S}_o$ , (B1) implies that the torque on  $\mathcal{S}_i$  is smaller than that on  $\mathcal{S}_o$ . The proof of this statement is similar to the one provided in [27] for the drag force. The actual velocity field, say  $\mathbf{u}_i$ , is the one induced by the rotation of  $\mathcal{S}_i$ , whereas  $\mathbf{u}_o$ , the velocity field induced by the rotation of  $\mathcal{S}_o$ , may be used for  $\mathbf{u}^*$ . Assuming that the fluid located in between the two surfaces rotates as a solid with the velocity field  $\boldsymbol{\Omega} \times \mathbf{x}$  implies that the associated dissipation rate is zero. This immediately yields  $T_i \leq T_o$ , where  $T_i$  and  $T_o$  denote the torques associated with the rotation of  $\mathcal{S}_i$  and  $\mathcal{S}_o$ , respectively. Consider now a circular cylinder with  $\chi = 1$ . A sphere of diameter  $D$  may be entirely enclosed within the cylinder, while a sphere of diameter  $2^{1/2}D$  completely encloses it. It follows that the torque  $T$  on the cylinder is such that  $\pi \mu D^3 \Omega \leq |T| \leq 2^{3/2} \pi \mu D^3 \Omega$ .

- [1] G. K. Batchelor, Slender-body theory for particles of arbitrary cross-section in Stokes flow, *J. Fluid Mech.* **44**, 419 (1970).
- [2] R. E. Khayat and R. G. Cox, Inertia effects on the motion of long slender bodies, *J. Fluid Mech.* **209**, 435 (1989).
- [3] G. B. Jeffery, The motion of ellipsoidal particles immersed in a viscous fluid, *Proc. Roy. Soc. London A* **102**, 161 (1922).
- [4] G. Subramanian and D. L. Koch, Inertial effects on fibre motion in simple shear flow, *J. Fluid Mech.* **535**, 383 (2005).
- [5] J. Einarsson, F. Candelier, F. Lundell, J.-R. Angilella, and B. Mehlig, Effect of weak fluid inertia upon Jeffery orbits, *Phys. Rev. E* **91**, 041002(R) (2015).
- [6] R. G. Cox, The steady motion of a particle of arbitrary shape at small Reynolds numbers, *J. Fluid Mech.* **23**, 625 (1965).
- [7] D. Lopez and E. Guazzelli, Inertial effects on fibers settling in a vortical flow, *Phys. Rev. Fluids* **2**, 024306 (2017).
- [8] A. Roy, R. J. Hamati, L. Tierney, D. L. Koch, and G. A. Voth, Inertial torques and a symmetry breaking orientational transition in the sedimentation of slender fibres, *J. Fluid Mech.* **875**, 576 (2019).
- [9] M. Shin and D. L. Koch, Rotational and translational dispersion of fibres in isotropic turbulent flows, *J. Fluid Mech.* **540**, 143 (2005).

- [10] G. A. Voth and A. Soldati, Anisotropic particles in turbulence, *Annu. Rev. Fluid Mech.* **49**, 249 (2017).
- [11] N. Pujara, G. A. Voth, and E. A. Variano, Scale-dependent alignment, tumbling and stretching of slender rods in isotropic turbulence, *J. Fluid Mech.* **860**, 465 (2019).
- [12] C. H. Ahn and M. G. Allen, Fluid micropumps based on rotary magnetic actuators, in *Proc. IEEE Micro Electro Mechanical Systems, 1995, MEMS '95* (IEEE, New York, 1995), pp. 408–412.
- [13] D. Chapple and S. Kresta, The effect of geometry on the stability of flow patterns in stirred tanks, *Chem. Eng. Sci.* **49**, 3651 (1994).
- [14] E. Loth, Drag of non-spherical solid particles of regular and irregular shape, *Powder Technol.* **182**, 342 (2008).
- [15] P. R. Kry and R. List, Aerodynamic torques on rotating oblate spheroids, *Phys. Fluids* **17**, 1087 (1974).
- [16] P. R. Kry and R. List, Angular motions of freely falling spheroidal hailstone models, *Phys. Fluids* **17**, 1093 (1974).
- [17] M. Kharrouba, J.-L. Pierson, and J. Magnaudet, Flow structure and loads over inclined cylindrical rodlike particles and fibers, *Phys. Rev. Fluids* **6**, 044308 (2021).
- [18] G. Mougouin and J. Magnaudet, The generalized Kirchhoff equations and their application to the interaction between a rigid body and an arbitrary time-dependent viscous flow, *Int. J. Multiphase Flow* **28**, 1837 (2002).
- [19] J. Magnaudet, M. Rivero, and J. Fabre, Accelerated flows past a rigid sphere or a spherical bubble. Part 1. Steady straining flow, *J. Fluid Mech.* **284**, 97 (1995).
- [20] J. B. Keller and S. I. Rubinow, Slender-body theory for slow viscous flow, *J. Fluid Mech.* **75**, 705 (1976).
- [21] J. C. R. Hunt, A. A. Wray, and P. Moin, Eddies, streams, and convergence zones in turbulent flows, Research Report CTR-S88, Center for Turbulence (1988).
- [22] T. A. Johnson and V. C. Patel, Flow past a sphere up to a Reynolds number of 300, *J. Fluid Mech.* **378**, 19 (1999).
- [23] L. G. Leal, *Advanced Transport Phenomena: Fluid Mechanics and Convective Transport Processes* (Cambridge University Press, Cambridge, 2007).
- [24] S. I. Rubinow and J. B. Keller, The transverse force on a spinning sphere moving in a viscous fluid, *J. Fluid Mech.* **11**, 447 (1961).
- [25] P. Gondret, M. Lance, and L. Petit, Bouncing motion of spherical particles in fluids, *Phys. Fluids* **14**, 643 (2002).
- [26] A. I. Korotkin, *Added Masses of Ship Structures* (Springer, New York, 2009).
- [27] R. Hill and G. Power, Extremum principles for slow viscous flow and the approximate calculation of drag, *Q. J. Mech. Appl. Math.* **9**, 313 (1956).
- [28] S. Kim and S. J. Karrila, *Microhydrodynamics: Principles and Selected Applications* (Butterworth-Heinemann, London, 1991).